

Mixed-metal Cu-Zn thiocyanate coordination polymers with melting behavior, glass transition, and tunable electronic properties

Chayanit Wechwithayakhlung,^{ab} Suttipong Wannapaiboon,^c Sutassana Na-Phattalung,^{de} Phisut Narabadeesuphakorn,^a Similan Tanjindaprateep,^a Saran Waiprasoet,^a Satoshi Horike,^{*ab} and Pichaya Pattanasattayavong^{*af}

^a Department of Materials Science and Engineering, School of Molecular Science and Engineering, Vidyasirimedhi Institute of Science and Technology (VISTEC), Rayong, 21210, Thailand

^b Institute for Integrated Cell-Material Sciences (iCeMS), Kyoto University, Kyoto 606-8501, Japan

^c Synchrotron Light Research Institute (Public Organization), 111 University Avenue, Muang District, Nakhon Ratchasima, 30000, Thailand

^d Division of Physics, School of Science, Walailak University, Nakhon Si Thammarat, 80160, Thailand

^e Functional Materials and Nanotechnology Center of Excellence, Walailak University, Nakhon Si Thammarat, 80160, Thailand

^f Research Network of NANOTEC-VISTEC on Nanotechnology for Energy, Vidyasirimedhi Institute of Science and Technology (VISTEC), Rayong, 21210, Thailand

* Corresponding authors. Email: pichaya.p@vistec.ac.th, horike@icems.kyoto-u.ac.jp

Abstract

The solid-state mechanochemical reactions under ambient conditions of CuSCN and Zn(SCN)₂ resulted in two novel materials: partially Zn-substituted α -CuSCN and a new phase Cu_xZn_y(SCN)_{x+2y}. The reactions take place at the labile S-terminal, and both products show melting and glass transition behaviors. The optical band gap and solid-state ionization potential can be adjusted systematically by adjusting the Cu:Zn ratio. Density functional theory calculations also reveal that the Zn-substituted CuSCN structure features a complementary electronic structure of Cu 3d states at the valence band maximum (VBM) and Zn 4s states at

the conduction band minimum (CBM). This work shows a new route to develop semiconductors based on coordination polymers which are becoming technologically relevant for electronic and optoelectronic applications.

Keywords: coordination polymers, semiconductors, mechanochemical reactions, electronic structures

Introduction

The ambidentate thiocyanate (SCN^-) ligand can coordinate with either hard or soft metal atoms and serve as either a bridging or terminal ligand.¹⁻³ Once studied mostly for structural coordination chemistry, the applications of metal thiocyanates (MSCN) in electronic and optoelectronic devices are emerging rapidly. For example, the thiocyanate (SCN^-) ligand was employed for the electronic properties tuning of the light-absorbing molecules in dye-sensitized solar cells (DSCs), of which SCN-bonded Ru dyes became the key players.⁴⁻⁷ More recently, copper(I) thiocyanate (CuSCN) has proved to be one of the highly promising transparent hole-transporting semiconductors, exhibiting wide-ranging applications in thin-film transistors (TFTs),^{8,9} organic light-emitting diodes (OLEDs),^{10,11} and various types of solar cells: DSCs,^{12,13} extremely-thin absorber (ETA) solar cells,^{14,15} quantum dot-sensitized solar cells (QDSCs),^{16,17} organic photovoltaics (OPVs),^{18,19} and perovskite solar cells (PSCs).²⁰⁻²³

The key attributes of CuSCN are its optical transparency and hole-transporting ability (p -type conductivity), resulting from the electronic structure comprising mainly $\text{Cu}^I 3d^{10}$ states hybridized with S $3p$ at the valence band maximum (VBM) and high-energy $\text{SCN}^- \pi^*$ states at the conduction band minimum (CBM).^{24,25} Compared to oxygen-bonded ligands, the improved energy matching between metal and sulfur atoms can provide efficient charge transport pathway in coordination polymers (CPs);²⁶⁻²⁸ indeed the structure of CuSCN can be visualized as 2D Cu-S sheets connected via CN bridges. Furthermore, we recently showed that tin(II) thiocyanate [$\text{Sn}(\text{SCN})_2$] is another transparent CP-based semiconductor with the VBM

dominated by S 3*p* and N 2*p* states with contributions from Sn^{II} 5*s*² lone pair electrons and can be used as an ultrathin anode interlayer in OPVs.^{29,30} Sn(SCN)₂ was also employed as a dopant in an electron transport layer that led to significant enhancements in OPV and PSC efficiencies.³¹ These examples clearly show that thiocyanate CPs have strong potential for electronic applications. Advances in the development of MSCN CPs can also contribute material design guidelines to the field of electrically conductive metal-organic frameworks (MOFs),^{32–34} which is a hot topic in the research community and has begun to move toward practical electronic applications.^{35–38}

The electronic states of MSCN CPs can be adjusted systematically by changing the metal centers. One compound of particular interest is zinc(II) thiocyanate [Zn(SCN)₂] which exhibits an electronic structure complementary to that of CuSCN. In the triclinic Zn(SCN)₂ structure,³⁹ the empty 4*s* states of Zn^{II} form the CBM below SCN⁻ π* states whereas the VBM features the ligand states only.⁴⁰ The excellent electron-transporting properties (*n*-type conductivity) of semiconducting oxides based on Zn or In are well-known and attributed to the spherical *s* orbitals forming the CBM states.^{41,42} In fact, the combination of such an *n*-type oxide with a Cu^I-based *p*-type semiconductor has only been demonstrated recently for high-performance electronic applications.^{43,44} An interesting question therefore arises: can we create mixed Cu-Zn thiocyanate compounds that would combine Cu^I 3*d* states at the VBM and Zn^{II} 4*s* states at the CBM? Such combination could potentially lead to the construction of various electronic devices, such as ambipolar transistors,⁴⁵ complementary circuits,⁴⁶ or *p-n* junction devices,⁴⁷ based on CP semiconductors.

Due to the structural versatility of the SCN⁻ ligand, heterometallic or mixed-metal thiocyanate CPs have been reported. For example, current attention on perovskite structures have led to interest in novel thiocyanate analogues: perovskite CsCd(SCN)₃,⁴⁸ double perovskite (NH₄)₂NiCd(SCN)₆,⁴⁹ and Prussian blue (A-site vacancy double perovskite) M^{III}Bi(SCN)₆ (M = Fe, Cr, Sc).⁵⁰ Importantly, there are specific examples that include Zn as bimetallic thiocyanate CPs of group 12 metals, such as ZnCd(SCN)₄ and ZnHg(SCN)₄, which

have been explored for their non-linear optical properties.^{51–54} The two metal sites are both tetrahedrally coordinated but distinct: one site bonded to 4 N (MN_4), the other to 4 S (MS_4). In the triclinic structure of $Zn(SCN)_2$,³⁹ there also exist two Zn coordination environments: ZnN_4 and ZnS_4 (depicted as part of Fig. 1). As Cu^I also has a tetrahedral geometry and can coordinate via both S and N, our motivation is therefore to explore the possibility of creating mixed Cu-Zn MSCN CPs that would yield electronic states from the metal centers at both VBM and CBM from Cu^I 3d and Zn^{II} 4s, respectively. To the best of our knowledge, such compounds have not been reported, and their discovery could open up a new compositional and/or structural space for further development of thiocyanate-based CP semiconductors.

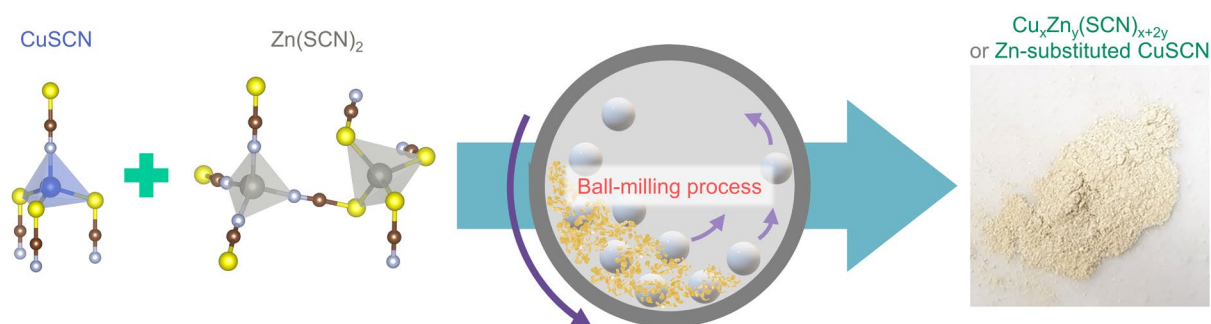


Fig. 1 Schematic diagram showing the combination of $CuSCN$ and $Zn(SCN)_2$ by a mechanochemical method to obtain $Cu_xZn_y(SCN)_{x+2y}$ and partially Zn-substituted $CuSCN$.

Herein, we employed a solid-state mechanochemical method to combine $CuSCN$ and $Zn(SCN)_2$ at various mixing ratios and obtained a new bimetallic $Cu_xZn_y(SCN)_{x+2y}$ phase as well as (partially) Zn-substituted $CuSCN$ for the first time (Fig. 1). The mechanochemical synthesis is a solvent-free reaction, allowing a direct combination of cations in SCN-based frameworks of which conventional solution synthesis cannot obtain.⁵⁵ The optical properties and electronic levels of the mixed compounds can be systematically tuned by varying the Cu:Zn ratio. Remarkably, the products also display melting and glass transition behaviors; the

liquid and glassy states of CPs are gaining immense research interest in recent years.⁵⁶⁻⁵⁸ We also employed density functional theory to study the electronic properties of the partially Zn-substituted CuSCN and found that the complementary electronic structure of Cu 3d VBM and Zn 4s CBM can be realized.

Structural and thermal analyses

The methods section is included in the Supplementary Information. Prior to reacting CuSCN and Zn(SCN)₂ together, each of the precursors was ball-milled separately to see the effects of mechanical grinding on their crystal structures. The powder X-ray diffraction (PXRD) results of the ball-milled precursors, denoted as BM-Cu for CuSCN and BM-Zn for Zn(SCN)₂, are included in Fig. 2a, which shows that their crystallinity can be broken down as seen from the broader XRD patterns. For CuSCN, the structure was also transformed from the rhombohedral (3R) β -phase (ICSD 24372)⁵⁹ to the orthorhombic α -phase (ICSD 124)⁶⁰ following the grinding step (Fig. S1a, Supplementary Information). Consequently, the mechanochemical reactions of CuSCN and Zn(SCN)₂ were carried out for different Cu(x):Zn(y) atomic ratios. The products, designated as **Cu_xZn_y**, appear as fine pale-yellow powder, which is different from the separately ball-milled precursors; BM-Cu appears light gray whereas BM-Zn appears pale pink. At an optimum ratio of 2:1 (**Cu₂Zn₁**), all starting materials were completely converted into the product as evident from the absence of PXRD signals of the pristine precursors (discussed below), suggesting good reactivity of CuSCN and Zn(SCN)₂.

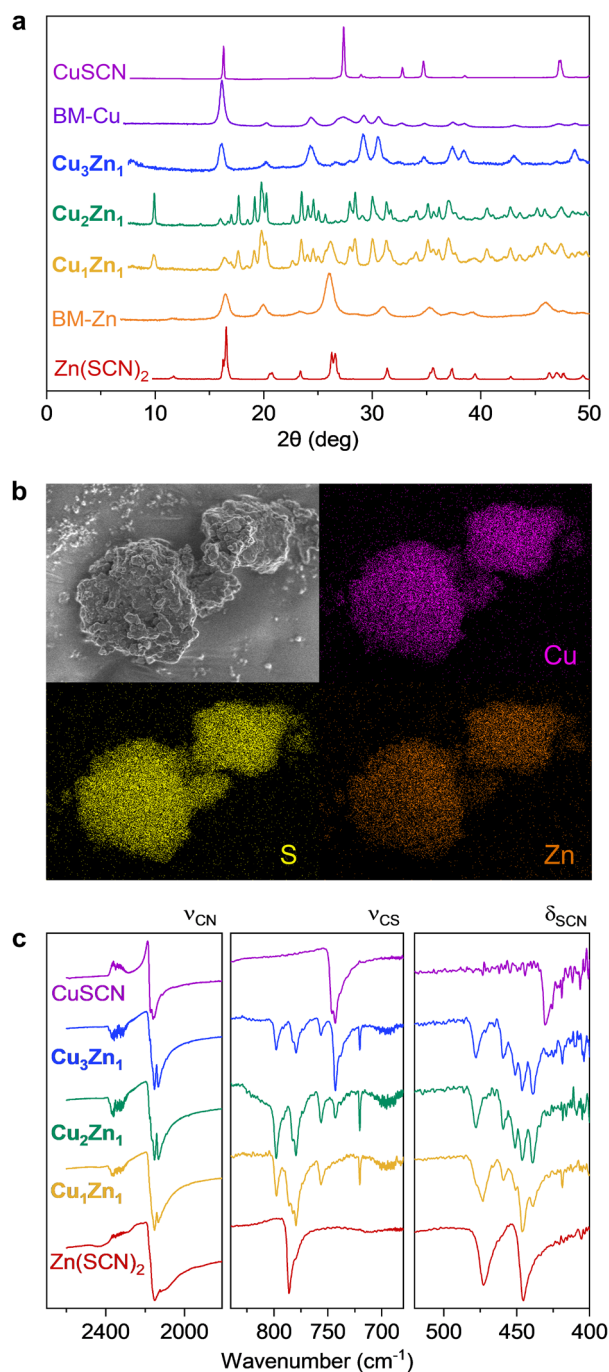


Fig. 2 (a) PXRD data of CuSCN and Zn(SCN)₂ precursors, their ball-milled powders (BM-Cu and BM-Zn, respectively), and **Cu_xZn_y** products where x:y is the Cu:Zn atomic ratio. (b) SEM image and EDX analysis of **Cu₂Zn₁** sample. (c) FTIR spectra.

The structural properties of the products were studied by PXRD as shown in Fig. 2a. We note that in addition to 3:1, 2:1, and 1:1 ratios displayed in the figure, other ratios with

higher Cu proportion (5.79:1) or higher Zn proportion (1:2 and 1:3) were also attempted, and the results are included in Fig. S1b. For Cu-rich samples where $x:y \geq 3:1$ (**Cu₃Zn₁** and **Cu_{5.79}Zn₁**), the PXRD data can be identified as the α -CuSCN phase without any detectable signals of Zn(SCN)₂. The preferred crystalline orientation changes from (200)-dominant in BM-Cu to (121)- and (112)-oriented in the mixed samples. This may suggest that mixing with Zn^{II} can disrupt the ordering along the longitudinal direction of the SCN⁻ ligand (*a*-axis) which is more directional compared to the M–S network in the *bc*-plane (Fig. S1b, inset). On the other hand, for **Cu₂Zn₁** sample, the PXRD result shows a distinct diffraction pattern which is indicative of a new phase, labelled as the copper-zinc thiocyanate (CZT) structure. The larger number of diffraction peaks may imply the alteration of crystal packing to a space group possessing a lower symmetry. When the proportion of Zn was increased further (**Cu₁Zn₁**, **Cu₁Zn₂**, and **Cu₁Zn₃**), some PXRD signals of Zn(SCN)₂ precursor can also be detected, suggesting the co-existence of CZT and Zn(SCN)₂ structures. Furthermore, **Cu_{5.79}Zn₁**, as an example of a sample with the α -CuSCN structure, was exposed to 85% relative humidity at 80 °C for 3 h and was found to convert to a mixture of CZT structure and α -CuSCN as shown in Fig. S1c. The PXRD intensity of the CZT structure was also observed to increase following the water vapor exposure.

By examining **Cu₂Zn₁** sample (CZT structure) with a scanning electron microscope (SEM), we observe that it consists of irregular-shaped particles with a broad size distribution (Fig. 2b). Energy-dispersive X-ray spectroscopy (EDX) shows homogeneous distributions of Cu, Zn, and S elements (also Fig. 2b), confirming that CZT is not a mixture and should be categorized as a new phase. Table S1 lists the atomic ratios of Cu, Zn, and S obtained from the EDX measurements. To compare with the nominal ratios from the synthesis, the data are normalized to the expected Cu atomic fraction. The trend in the ratios of Zn and S changes according to the expectation, but their values are lower than the nominal values. Zn is found to be 10-20% less than expected, possibly due to the overlap of Cu and Zn L _{α} X-ray emissions leading to experimental errors. S is found to be consistently 30-40% lower than expected,

likely due to the loss of sulfur from sublimation in high vacuum during the measurements.⁶¹ Fig. 2c displays the Fourier-transform infrared spectroscopy (FTIR) spectra of Cu_xZn_y samples in the relevant spectral ranges of CN stretching (ν_{CN} , 2000-2200 cm^{-1}), CS stretching (ν_{CS} , 700-825 cm^{-1}), and SCN bending (δ_{SCN} , 400-500 cm^{-1}).^{62,63} ν_{CN} mode remains qualitatively similar for all samples whereas ν_{CS} displays drastic changes, indicating that the S-terminal of SCN^- is likely more labile which allows the solid-state reaction to take place. Peak splittings in the ν_{CS} and δ_{SCN} spectral ranges of Cu_xZn_y products are also evident, which could be related to the SCN^- coordinating with two different metal cations. The results confirm that the SCN^- are intact and that new bonding environments are formed due to the mechanochemical reaction of CuSCN and $\text{Zn}(\text{SCN})_2$.

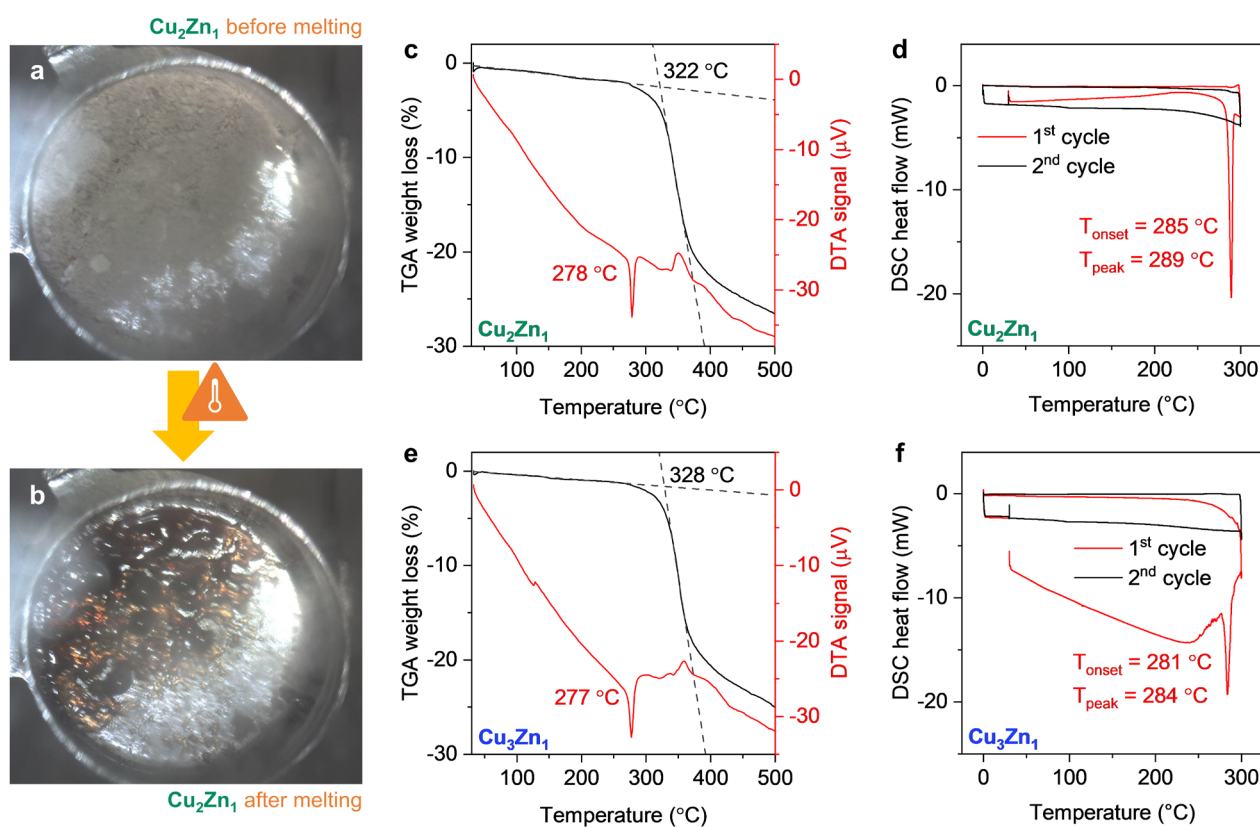


Fig. 3 (a, b) Photographs of Cu_2Zn_1 sample before and after melting, taken during the TG-DTA measurement. (c, d) TG-DTA and DSC results of Cu_2Zn_1 sample. (e, f) TG-DTA and DSC results of Cu_3Zn_1 sample.

Considering the thermal properties, the parent compounds CuSCN and Zn(SCN)₂ decompose at 408 and 393 °C, respectively, as seen from the thermogravimetry-differential thermal analysis (TG-DTA) results (Fig. S2a-b). Interestingly, Zn(SCN)₂ shows melting behavior, observed as an endothermic peak at 221 °C in Fig. S2b and visually in the photographs shown in Fig. S2c-d. The melting of Zn(SCN)₂ has not been reported before, and its thermal characteristics suggest that the coordination bonds in Zn(SCN)₂ can be broken more easily compared to CuSCN. In fact, many CPs that melt upon heating also consist of Zn^{II}.^{57,58} When mixed together, **Cu_xZn_y** samples decompose at lower temperatures (< 330 °C) and, remarkably, exhibit melting behavior in both Zn-mixed α-CuSCN and CZT structures. The photographs before and after the melting of **Cu₂Zn₁** (CZT structure) are shown in Fig. 3a-b while the TG-DTA and differential scanning calorimetry (DSC) results are plotted in Fig. 3c-d, clearly displaying the melting behavior that occurs in the 280-290 °C range. For **Cu₁Zn₁** sample which contains mixed CZT and Zn(SCN)₂ structures (see PXRD results in Fig. 2a), two melting instances are observed (Fig. S2e); the first one at 198 °C is likely due to the co-existing Zn(SCN)₂ phase whereas the second peak at 290 °C can be ascribed to the CZT phase. Similarly, the α-CuSCN phase when containing Zn^{II} in the structure also exhibits melting behavior in the same temperature range as can be seen from the results of **Cu₃Zn₁** shown in Fig. 3e-f. Even at a lower concentration of Zn (**Cu_{5.79}Zn₁**), the melting still occurs (Fig. S2f), further emphasizing that Zn^{II} can promote the solid-to-liquid phase transition. From the DSC experiments, the **Cu_xZn_y** products transform into an amorphous, glassy state following the first heating as evident from the occurrence of glass transition during the second heating around 90 °C as shown in Fig. S3.

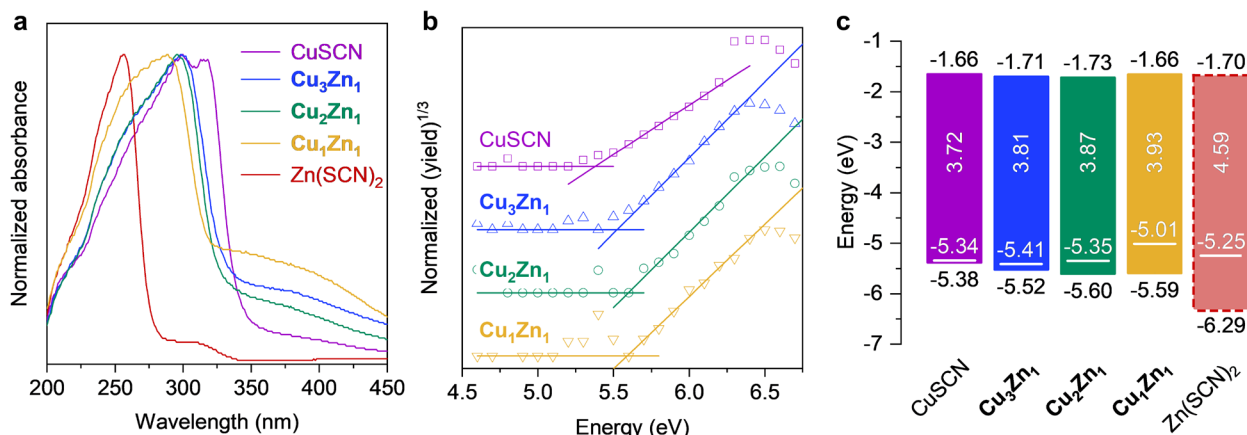


Fig. 4 (a) Optical absorbance spectra of powder samples. (b) Photoelectron yield^{1/3} spectra for the determination of the valence band edge. (c) Simple band diagrams showing the E_g^{opt} , VBM, CBM, and E_F .

Optical and electronic properties

The optical properties of the samples were studied by diffuse reflectance spectroscopy. The optical absorption spectra were calculated from the reflection spectra using the Kubelka-Munk model as plotted in Fig. 4a, and the optical band gaps (E_g^{opt}) were calculated from Tauc plots (Fig. S4). The main absorption peak is blue-shifted from 315 nm for CuSCN to 256 nm for Zn(SCN)₂, accompanied by an increase of E_g^{opt} with the increasing proportion of Zn from 3.72 eV for CuSCN to 4.59 eV for Zn(SCN)₂. The energetic positions of the VBM, i.e., the solid-state ionization potentials, were obtained from photoelectron yield spectroscopy (PYS) and found to descend deeper with respect to the vacuum level also with the increasing proportion of Zn as shown in Fig. 4b. The simplified energy band diagrams with data of E_g^{opt} , VBM, CBM (CBM = VBM + E_g^{opt}), and Fermi level (E_F , measured by Kelvin probe) are shown in Fig. 4c. We note that the VBM of Zn(SCN)₂ was out of range of our PYS instrument and could not be measured directly. However, the results from the other samples in Fig. 4c show that the CBM level does not vary significantly; this is likely due to electronic states in the conduction bands being dominated by the SCN π^* states which were present in all samples. This agrees with

our previous theoretical study of CuSCN and $\text{Zn}(\text{SCN})_2$ (although there are Zn^{II} states below the SCN π^* states in $\text{Zn}(\text{SCN})_2$, the density of states is significantly lower).⁴⁰ We therefore reason that the CBM level of $\text{Zn}(\text{SCN})_2$ should be close to those of other samples around 1.70 eV, and the VBM can be obtained from $\text{CBM} - E_g^{\text{opt}}$ in this case. The inclusion of Zn^{II} also shifts E_F away from the VBM, agreeing with the fact that Zn^{II} contributes 4s states to the CBM (discussed in the section on computational study). The systematic shifts in the energy levels as a function of Zn proportion show that mixing with $\text{Zn}(\text{SCN})_2$ is one promising method to tune the electronic properties of CuSCN.

Local environments of Cu and Zn

To investigate the local coordination environment, the samples were characterized by X-ray absorption spectroscopy (XAS) at beamline BL1.1W, Synchrotron Light Research Institute (SLRI), Thailand. The XAS spectra at Cu K-edge and Zn K-edge were recorded in both X-ray absorption near edge structure (XANES) and extended X-ray absorption fine structure (EXAFS) regions as shown in Fig. 5, and the analyzed EXAFS data in k-space and R-space are shown in Fig. S5. First, we observe that the ball-milling process does not alter the local Cu and Zn environments of pristine CuSCN and $\text{Zn}(\text{SCN})_2$. Specifically, the phase transition of BM-Cu with respect to pristine CuSCN upon grinding leads to the alteration of crystal packing (change in XRD pattern) but does not alter the local structure of Cu (Fig. 5a and Fig. S5a-b). In the case of BM-Zn, both PXRD and XAS data are matched well with the pristine $\text{Zn}(\text{SCN})_2$ indicating that only the pulverization of bulk particles into smaller particles upon grinding occurred. Moreover, Cu and Zn are confirmed to be in +1 and +2 oxidation states, respectively, in all samples as evident from the XANES spectra. Upon ball-milling of the mixed metal precursors, the Cu K-edge EXAFS spectra of all samples with varying Cu:Zn ratio appear similar to that of BM-Cu, indicating a similar local structure of Cu. This observation suggests that there is no significant modification of the Cu local environment in CuSCN, BM-Cu, and Cu_xZn_y samples.

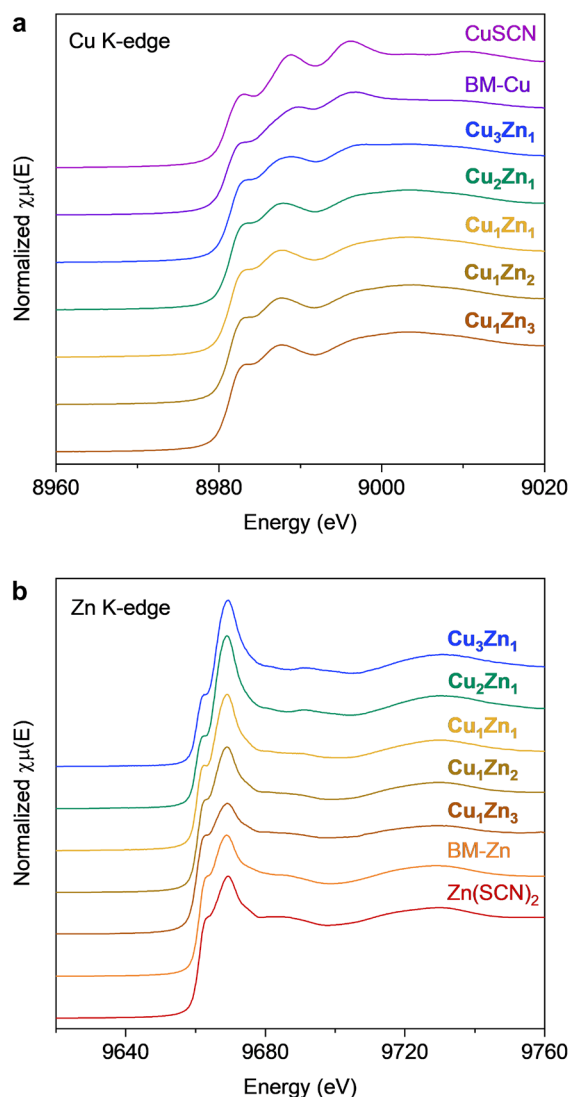


Fig. 5 XAS spectra at (a) Cu K-edge and (b) Zn K-edge in both XANES and EXAFS regions.

On the contrary, the Zn K-edge EXAFS spectra of the Cu_xZn_y products vary with the x:y ratio (Fig. 5b and Fig. S5c-d). The Zn K-edge spectra of Cu_3Zn_1 and Cu_2Zn_1 samples are similar to each other even though their PXRD patterns are different. In Cu_3Zn_1 which has the α -CuSCN-based structure, Zn likely exists as a substitutional defect since the crystal ionic radii of Cu^{I} and Zn^{II} , both in the tetrahedral coordination geometry in thiocyanate compounds, are the same: 0.74 Å.⁶⁴ Our computational study also confirms that the Zn-substitutional defect can form in α -CuSCN as discussed in the next section. Although Cu_2Zn_1 has a crystal structure of the new CZT phase, the local Zn environment is similar to that of Cu_3Zn_1 , characterized by

two peaks approximately at 1.5 and 2.5 Å in the R-space data (Fig. S5d). We also note the correspondence of FTIR spectra between the Cu_3Zn_1 and Cu_2Zn_1 samples as shown in Fig. 2c, further highlighting the similarity of the bonding environments in the two different crystal structures. This implies that the local environments in the CZT structure is possibly based on that of α -CuSCN as well, but the crystal structure differs in terms of packing and symmetry. When the Zn atomic fraction increases (Cu_1Zn_1 , Cu_1Zn_2 , and Cu_1Zn_3), there is an additional peak at 2 Å in the R-space data which coincides with the spectra of BM-Zn and $\text{Zn}(\text{SCN})_2$. This is in agreement with the PXRD data which show that these samples were mixtures of CZT and $\text{Zn}(\text{SCN})_2$ phases.

Computational study of Zn-substituted α -CuSCN

Following the identification of the potential existence of Zn-substitutional defect at Cu sites (Zn_{Cu}) in α -CuSCN, we performed DFT calculations to study its formation energy and the effects on the electronic properties. The concentration (C) of a defect (D) under thermodynamic equilibrium can be determined by

$$C(D^q) = \exp\left[-\frac{E^f(D^q)}{k_B T}\right] \quad (1),$$

where $E^f(D^q)$ is the formation energy of defect D in a charge state q , k_B is the Boltzmann constant, and T is the temperature. This equation shows the inverse relationship between the concentration of a defect and the defect formation energy. The latter is defined as^{65,66}

$$E^f = E_{\text{tot}}(D^q) - E_{\text{tot}}(0) + \sum \Delta n_x \mu_x + q E_F \quad (2),$$

where $E_{\text{tot}}(D^q)$ is the total energy of the cell containing defect D in a charge state q , $E_{\text{tot}}(0)$ is the total energy of bulk α -CuSCN without any defects, Δn_x is the number of an atom of species X being removed (positive) or added (negative) to the cell, μ_x is the chemical potential of an atom of species X , and E_F is the Fermi energy. In this study, the chemical potentials μ of Cu and Zn were set to the values of their natural phases, which are fcc Cu and hcp Zn. It is worth

noting that although the rough approximations of these chemical potentials are expected to be different from those obtained by determining alternative phases that are favorable under extreme growth conditions, these values are still useful as a first approximation to calculate the formation energy.

We performed the calculations for α -CuSCN with one Cu position (out of eight Cu atoms in a unit cell) substituted with a Zn atom, so called a point defect. Two charge states of $q = 0$ and $+1$ (Zn_{Cu}^0 and Zn_{Cu}^+ , respectively) were found to be stable. We note that Zn_{Cu}^0 and Zn_{Cu}^+ correspond to Zn in the oxidation states of Zn^I and Zn^{II} , respectively. Specifically, if Cu^I is substituted with Zn^I , the defect is in the neutral charge state; when Cu^I is substituted with Zn^{II} , the defect has a charge of $+1$. The calculated formation energies as a function of E_F are shown in Fig. S6. In the plot, E_F is referenced to the VBM and varied from 0 eV and 3.82 eV, which is the calculated band gap of α -CuSCN from DFT employing the HSE06 hybrid exchange-correlation functional. The calculated band gap value agrees well with the experimental value found at 3.72 eV (Fig. 4c), verifying that the calculations with the HSE06 functional provide a more accurate band gap value than those with typical DFT exchange-correlation functionals, such as local density approximation (LDA) or generalized gradient approximation (GGA).

As seen in Fig. S6, the formation energy of Zn_{Cu}^+ is lower than that of Zn_{Cu}^0 for most of the E_F range ($E_F < 3.04$ eV) and becomes negative for $E_F < 0.87$ eV. This suggests that the formation of Zn_{Cu}^+ is spontaneous when α -CuSCN is under p -type condition which is the case for our samples as seen from the position of E_F being close to VBM (Fig. 4c). In addition, to verify the oxidation state of the Zn atom in the Zn_{Cu}^+ defect, we carried out the Bader charge analysis⁶⁷ and compared the Bader charge on Zn between ZnO and Zn_{Cu}^+ . We find that the calculated Bader charge on Zn in ZnO is $+1.15$ whereas that on Zn in Zn_{Cu}^+ is $+1.03$; the good agreement between the two cases suggest that they possibly have a similar oxidation state. As Zn in ZnO is known to be in the Zn^{II} oxidation state, Zn in Zn_{Cu}^+ is likely to be Zn^{II} as well. The calculations results support that Zn^{II} can substitute Cu^I in α -CuSCN, forming Zn_{Cu}^+ defects

without incurring an energy penalty. On the other hand, Zn_{Cu}^0 can be more stable (when compared to Zn_{Cu}^+) only when $E_F > 3.04$ eV, i.e., under *n*-type condition, which is not likely for CuSCN that is generally observed to display *p*-type conductivity.^{13,14,68} Therefore, Zn^I (which would give rise to Zn_{Cu}^0) is less likely to exist in our samples. The findings also corroborate well with the results from XANES measurements that show Cu and Zn exist as Cu^I and Zn^{II} in all samples as discussed in the previous section.

To investigate the effects of Zn_{Cu}^+ on the electronic structure of α -CuSCN, charge densities at the highest occupied state and lowest unoccupied state (i.e., at the VBM and CBM, respectively) as well as the total density of states (DOS) and partial DOS (pDOS) were calculated for both bulk α -CuSCN and α -CuSCN with Zn_{Cu}^+ . Comparing the charge densities of former (Fig. 6a-b) against those of the latter (Fig. 6c-d), the electronic states of substitutional Zn^{II} are featured specifically at the CBM and not at all at the VBM. DOS and pDOS plotted in Fig. 6e also show that the VB of α -CuSCN is minimally affected by the Zn-substitution and retains the Cu *3d*-dominant character. In contrast, the CB shows defect-induced states derived from Zn *4s* states below the CBM. Importantly, Zn_{Cu}^+ does not lead to any defect levels within the band gap that would otherwise act as deep trapping states. In fact, Zn *4s* is delocalized via the hybridization with C and N *2p* states, evident from the charge distribution over Zn, C, and N at the CBM as illustrated in Fig. 6d. Furthermore, Zn_{Cu}^+ can be classified as an electron donor state due to its presence at the CBM. Each substitutional Zn^{II} donates 1 extra electron (compared to Cu^I in the host lattice) to the conduction band of α -CuSCN and simultaneously forms an ionized donor state with +1 charge, hence the charge neutrality is maintained. The electron donation is also reflected in the shift of E_F away from the VB edge of α -CuSCN when Zn is added as observed in the experimental results (Fig. 4c).

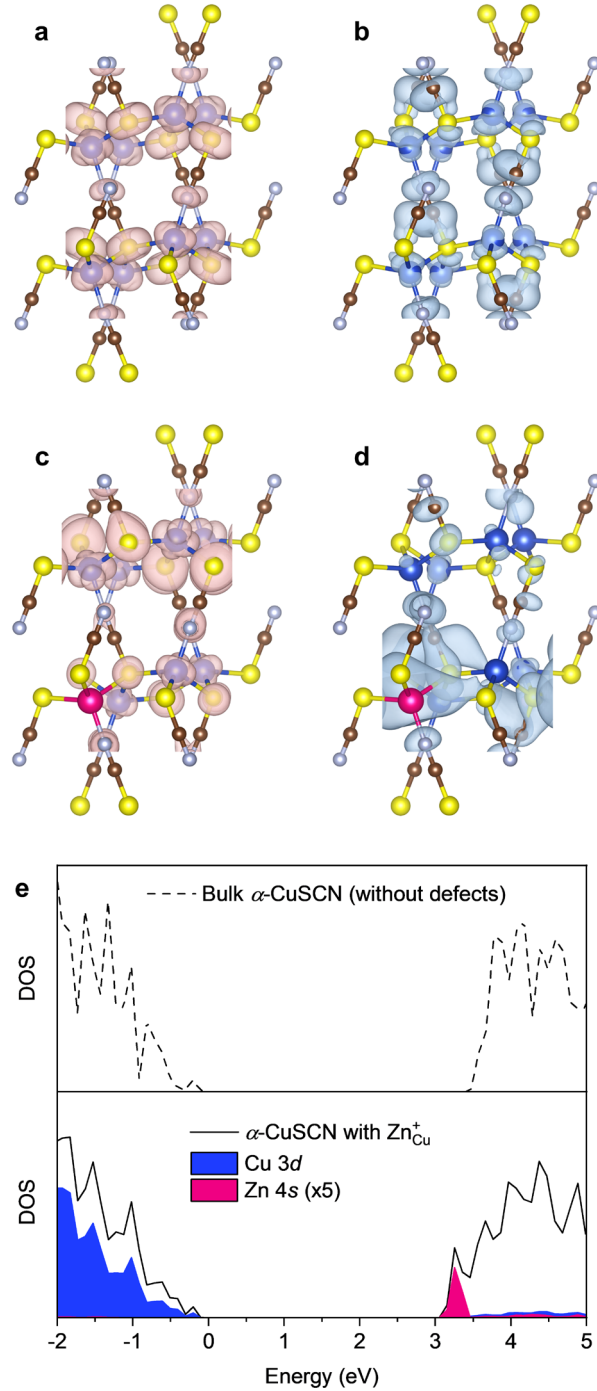


Fig. 6 Illustrations of charge densities of bulk α -CuSCN (without defects) at (a) the highest occupied state and (b) the lowest unoccupied state in comparison with the charge densities of α -CuSCN with Zn_{Cu}^+ also at (c) the highest occupied state and (d) the lowest unoccupied state. The blue, pink, yellow, brown, and grey spheres refer to Cu, Zn, S, C, and N, respectively. (e) Total and site-decomposed electron density of state (DOS), where the dashed and solid lines are the total DOS of bulk α -CuSCN and of α -CuSCN with Zn_{Cu}^+ , respectively. The blue and pink shaded area are the partial DOS of Cu 3d and Zn 4s states, respectively. Note that the DOS on the Zn atom is scaled up by a factor of 5 for clarity.

Discussions

Based on the results presented in this work, we surmise that during the mechanochemical reaction, the $\text{Zn}(\text{SCN})_2$ structure can be broken down (also evident from its melting behavior), after which Zn^{II} can be incorporated into the α -CuSCN structure which is more rigid. The similar crystal ionic radii and coordination geometry between Cu^{I} and Zn^{II} allow the two metal ions to mix. When Cu is in excess ($\text{Cu}_{5.79}\text{Zn}_1$ and Cu_3Zn_1), the main structure of α -CuSCN is retained in which Zn^{II} exists as a substitutional defect (Zn_{Cu}). The computational study by DFT also finds that Zn_{Cu} in +1 charge state is stable with low formation energies especially when E_{F} is close to VBM (p -type condition), which is the case for our samples. However, when the ratio is 2:1 (Cu_2Zn_1), the large number of defect sites likely increases the crystal energy such that the orthorhombic packing of α -CuSCN is no longer stable, transforming into a low-symmetry space group—the CZT structure—with a nominal chemical formula of $\text{Cu}_2\text{Zn}(\text{SCN})_4$. A further increase in the Zn atomic fraction results in the co-existence of CZT and $\text{Zn}(\text{SCN})_2$ structures, suggesting that the CZT phase may be at the boundary for homogeneous mixing between Cu^{I} and Zn^{II} in the thiocyanate compound.

Importantly, the substitution of Cu^{I} with Zn^{II} leads to the presence of Zn^{II} 4s orbitals at the CBM of α -CuSCN, forming delocalized states via the hybridization with C and N 2p states. As a result, Zn_{Cu}^+ becomes a donor state that shifts E_{F} away from VBM toward midgap. With the top of the VB still formed mostly by Cu^{I} 3d, α -CuSCN with Zn_{Cu}^+ shows a novel electronic structure with metal-dominant character at both VBM and CBM. Mixing Cu/Zn in the thiocyanate compounds is shown as an effective method to systematically tune the optical and electronic properties. As CuSCN has been demonstrated as a highly promising semiconductor, this method could offer a novel route to fine-tuning the electronic levels, for example the VBM and E_{F} levels, to match with the energy levels of other layers in thin-film electronic devices.

Another remarkable point is the observation of the melting behavior of Cu_xZn_y products. Crystal melting of CPs is rare,⁵⁶ and such behavior of CuSCN-based CPs has only

recently been discovered. In the previous work, CuSCN was modified with 4,4'-bipyridin-1-ium derivatives to allow melting behavior.⁶⁹ In our current system, the melting is realized by combining two metal cations with different oxidation states, Cu^I and Zn^{II}. As both are tetrahedrally coordinated with thiocyanate ligands, the charge difference may also affect electrostatic interactions and reduce lattice potential energies, leading to the emergence of melting behavior and glassy state. This would allow a novel solvent-free method for the deposition of CuSCN-based semiconductors. Further investigations should look at how much Zn doping is required to allow melting as well as characterize the electronic properties of melt-processed CuSCN-based thin films.

Conclusions

Starting from CuSCN and Zn(SCN)₂, we applied the mechanochemical synthesis method to successfully obtain new materials: (1) partially Zn-substituted α -CuSCN and (2) a new bimetallic CZT structure. The solid-state reaction occurs at the more labile S-coordination sites, and the resulting products show melting behavior and glass transition. Both structures are ambient-stable and comprise mixed-valence metal cations, Cu^I and Zn^{II}. With respect to CuSCN, E_g^{opt} widens, VBM deepens, and E_F shifts away from VBM with the increasing amount of Zn. DFT calculations reveal that α -CuSCN containing Zn_{Cu}⁺ features electronic states of metals at both the VBM and CBM from Cu 3*d* and Zn 4*s*, respectively. This work also demonstrates that CuSCN can be made melt-processable by mixing with Zn(SCN)₂ and that the optical and electronic properties of CuSCN can be systematically tuned by adjusting the proportion of Zn in the structure.

Author contributions

CRedit descriptions. **Chayanit Wechwithayakhlung**: Methodology, Investigation, Data curation, Formal analysis, Visualization, and Writing – original draft. **Suttipong**

Wannapaiboon: Methodology, Formal analysis, Validation, and Writing – review & editing (XANES and EXAFS experiments). **Sutassana Na-Phattalung:** Methodology, Supervision, Validation, and Writing – review & editing (DFT calculations). **Phisut Narabadeesuphakorn, Similan Tanjindaprateep,** and **Saran Waiprasoet:** Investigation (XANES and EXAFS experiments). **Satoshi Horike:** Conceptualization, Funding acquisition, Resources, Supervision, and Writing – review & editing. **Pichaya Pattanasattayavong:** Conceptualization, Funding acquisition, Resources, Project administration, Supervision, Validation, Visualization, and Writing – review & editing.

Conflicts of interest

There are no conflicts of interest to declare.

Acknowledgements

This research was supported by grant TRG6280013 jointly funded by Thailand's Synchrotron Light Research Institute (SLRI) and Thailand Research Fund (TRF) and grant FRB640087 funded by Thailand Science Research and Innovation (TSRI). C.W. and P.P. acknowledge Vidyasirimedhi Institute of Science and Technology for financial support. C.W., S.H. and P.P. also acknowledge funding from iCeMS-VISTEC Smart Materials Research Center. S.N. was supported by Thailand Science Research and Innovation Fund, contract number WU-FF64101. Synchrotron Light Research Institute, Thailand, is also acknowledged for the provision of XAS beamtime at the Beamline 1.1W (Multiple X-ray Techniques, MXT). The authors also thank Dr. Daniel Packwood from iCeMS, Kyoto University, for valuable advice and computational resources.

References

- 1 A. H. Norbury, *Adv. Inorg. Chem. Radiochem.*, 1975, **17**, 231–386.
- 2 J. Burmeister, *Coord. Chem. Rev.*, 1990, **105**, 77–133.
- 3 M. Kabešová, R. Boča, M. Melník, D. Valigura and M. Dunaj-Jurčo, *Coord. Chem. Rev.*, 1995, **140**, 115–135.
- 4 M. K. Nazeeruddin, A. Kay, I. Rodicio, R. Humphry-Baker, E. Mueller, P. Liska, N. Vlachopoulos and M. Graetzel, *J. Am. Chem. Soc.*, 1993, **115**, 6382–6390.
- 5 M. K. Nazeeruddin, P. Péchy and M. Grätzel, *Chem. Commun.*, 1997, **1**, 1705–1706.
- 6 M. K. Nazeeruddin, P. Péchy, T. Renouard, S. M. Zakeeruddin, R. Humphry-Baker, P. Comte, P. Liska, L. Cevey, E. Costa, V. Shklover, L. Spiccia, G. B. Deacon, C. A. Bignozzi and M. Grätzel, *J. Am. Chem. Soc.*, 2001, **123**, 1613–1624.
- 7 M. K. Nazeeruddin, S. M. Zakeeruddin, R. Humphry-Baker, M. Jirousek, P. Liska, N. Vlachopoulos, V. Shklover, C.-H. Fischer and M. Grätzel, *Inorg. Chem.*, 1999, **38**, 6298–6305.
- 8 P. Pattanasattayavong, N. Yaacobi-Gross, K. Zhao, G. O. N. Ndjawa, J. Li, F. Yan, B. C. O'Regan, A. Amassian and T. D. Anthopoulos, *Adv. Mater.*, 2013, **25**, 1504–1509.
- 9 P. Worakajit, F. Hamada, D. Sahu, P. Kidkhunthod, T. Sudyoadsuk, V. Promarak, D. J. Harding, D. M. Packwood, A. Saeki and P. Pattanasattayavong, *Adv. Funct. Mater.*, 2020, **30**, 2002355.
- 10 A. Perumal, H. Faber, N. Yaacobi-Gross, P. Pattanasattayavong, C. Burgess, S. Jha, M. A. McLachlan, P. N. Stavrinou, T. D. Anthopoulos and D. D. C. Bradley, *Adv. Mater.*, 2015, **27**, 93–100.
- 11 L. Xu, Y. Li, L. Chen, J. Wang, C. Zheng, Y. Qi, R. Chen and W. Huang, *ACS Sustain. Chem. Eng.*, 2018, **6**, 17178–17183.

- 12 K. Tennakone, K. P. Hewaparakkrama, M. Dewasurendra, A. H. Jayatissa and L. K. Weerasena, *Semicond. Sci. Technol.*, 1988, **3**, 382–387.
- 13 B. O'Regan and D. T. Schwartz, *Chem. Mater.*, 1995, **7**, 1349–1354.
- 14 K. Tennakone, G. R. R. A. Kumara, I. R. M. Kottegoda, V. P. S. Perera and G. M. L. P. Aponso, *J. Phys. D: Appl. Phys.*, 1998, **31**, 2326–2330.
- 15 C. Lévy-Clément, R. Tena-Zaera, M. a. Ryan, A. Katty and G. Hodes, *Adv. Mater.*, 2005, **17**, 1512–1515.
- 16 G. Larramona, C. Choné, A. Jacob, D. Sakakura, B. Delatouche, D. Péré, X. Cieren, M. Nagino and R. Bayón, *Chem. Mater.*, 2006, **18**, 1688–1696.
- 17 J. Briscoe, D. E. Gallardo, S. Hatch, V. Lesnyak, N. Gaponik and S. Dunn, *J. Mater. Chem.*, 2011, **21**, 2517.
- 18 N. Yaacobi-Gross, N. D. Treat, P. Pattanasattayavong, H. Faber, A. K. Perumal, N. Stingelin, D. D. C. Bradley, P. N. Stavrinou, M. Heeney and T. D. Anthopoulos, *Adv. Energy Mater.*, 2015, **5**, 1401529.
- 19 M. Li, K. Gao, X. Wan, Q. Zhang, B. Kan, R. Xia, F. Liu, X. Yang, H. Feng, W. Ni, Y. Wang, J. Peng, H. Zhang, Z. Liang, H.-L. Yip, X. Peng, Y. Cao and Y. Chen, *Nat. Photonics*, 2017, **11**, 85–90.
- 20 P. Qin, S. Tanaka, S. Ito, N. Tetreault, K. Manabe, H. Nishino, M. K. Nazeeruddin and M. Grätzel, *Nat. Commun.*, 2014, **5**, 3834.
- 21 S. Ye, W. Sun, Y. Li, W. Yan, H. Peng, Z. Bian, Z. Liu and C. Huang, *Nano Lett.*, 2015, **15**, 3723–3728.
- 22 N. Wijeyasinghe, A. Regoutz, F. Eisner, T. Du, L. Tsetseris, Y.-H. Lin, H. Faber, P. Pattanasattayavong, J. Li, F. Yan, M. A. McLachlan, D. J. Payne, M. Heeney and T. D. Anthopoulos, *Adv. Funct. Mater.*, 2017, **27**, 1701818.

- 23 N. Arora, M. I. Dar, A. Hinderhofer, N. Pellet, F. Schreiber, S. M. Zakeeruddin and M. Grätzel, *Science*, 2017, **358**, 768–771.
- 24 J. E. Jaffe, T. C. Kaspar, T. C. Droubay, T. Varga, M. E. Bowden and G. J. Exarhos, *J. Phys. Chem. C*, 2010, **114**, 9111–9117.
- 25 L. Tsetseris, *J. Phys.: Condens. Matter*, 2016, **28**, 295801.
- 26 B. J. Holliday and T. M. Swager, *Chem. Commun.*, 2005, 23.
- 27 L. Sun, T. Miyakai, S. Seki and M. Dincă, *J. Am. Chem. Soc.*, 2013, **135**, 8185–8188.
- 28 J. Xie, L. Wang and J. S. Anderson, *Chem. Sci.*, 2020, **11**, 8350–8372.
- 29 C. Wechwithayakhlung, D. M. Packwood, J. Chaopaknam, P. Worakajit, S. Ittisanronnachai, N. Chanlek, V. Promarak, K. Kongpatpanich, D. J. Harding and P. Pattanasattayavong, *J. Mater. Chem. C*, 2019, **7**, 3452–3462.
- 30 J. Chaopaknam, C. Wechwithayakhlung, H. Nakajima, T. Lertvanithphol, M. Horpratum, T. Sudyoadsuk, V. Promarak, A. Saeki and P. Pattanasattayavong, 2021, arXiv:2105.01024.
- 31 A. Seitkhan, M. Neophytou, M. Kirkus, E. Abou-Hamad, M. N. Hedhili, E. Yengel, Y. Firdaus, H. Faber, Y. Lin, L. Tsetseris, I. McCulloch and T. D. Anthopoulos, *Adv. Funct. Mater.*, 2019, **29**, 1905810.
- 32 T. C. Narayan, T. Miyakai, S. Seki and M. Dincă, *J. Am. Chem. Soc.*, 2012, **134**, 12932–12935.
- 33 M. E. Ziebel, L. E. Darago and J. R. Long, *J. Am. Chem. Soc.*, 2018, **140**, 3040–3051.
- 34 L. S. Xie, G. Skorupskii and M. Dincă, *Chem. Rev.*, 2020, **120**, 8536–8580.
- 35 G. Wu, J. Huang, Y. Zang, J. He and G. Xu, *J. Am. Chem. Soc.*, 2017, **139**, 1360–1363.

- 36 D. Y. Ahn, D. Y. Lee, C. Y. Shin, H. T. Bui, N. K. Shrestha, L. Giebeler, Y.-Y. Noh and S.-H. Han, *ACS Appl. Mater. Interfaces*, 2017, **9**, 12930–12935.
- 37 H. Arora, R. Dong, T. Venanzi, J. Zscharschuch, H. Schneider, M. Helm, X. Feng, E. Cánovas and A. Erbe, *Adv. Mater.*, 2020, **32**, 1907063.
- 38 H. Liu, Y. Wang, Z. Qin, D. Liu, H. Xu, H. Dong and W. Hu, *J. Phys. Chem. Lett.*, 2021, **12**, 1612–1630.
- 39 L. A. Aslanov, V. M. Ionov and K. Kynev, *Kristallografiya*, 1976, 21, 1198–1199.
- 40 C. Wechwithayakhlung, D. M. Packwood, D. J. Harding and P. Pattanasattayavong, *J. Phys. Chem. Solids*, 2021, **154**, 110085.
- 41 K. Nomura, H. Ohta, A. Takagi, T. Kamiya, M. Hirano and H. Hosono, *Nature*, 2004, **432**, 488–492.
- 42 K. Nomura, T. Kamiya, H. Ohta, K. Ueda, M. Hirano and H. Hosono, *Appl. Phys. Lett.*, 2004, **85**, 1993–1995.
- 43 A. Liu, H. Zhu, W.-T. Park, S.-J. Kang, Y. Xu, M.-G. Kim and Y.-Y. Noh, *Adv. Mater.*, 2018, **30**, 1802379.
- 44 A. Liu, H. Zhu, W.-T. Park, S.-J. Kim, H. Kim, M.-G. Kim and Y.-Y. Noh, *Nat. Commun.*, 2020, **11**, 4309.
- 45 L. Yan Liang, H. Tao Cao, X. Bo Chen, Z. Min Liu, F. Zhuge, H. Luo, J. Li, Y. Cheng Lu and W. Lu, *Appl. Phys. Lett.*, 2012, **100**, 263502.
- 46 P. K. Nayak, J. A. Caraveo-Frescas, Z. Wang, M. N. Hedhili, Q. X. Wang and H. N. Alshareef, *Sci. Rep.*, 2015, **4**, 4672.
- 47 Z. Wang, P. K. Nayak, A. Albar, N. Wei, U. Schwingenschlögl and H. N. Alshareef, *Adv. Mater. Interfaces*, 2015, **2**, 1500374.
- 48 G. Thiele and D. Messer, *Z. Anorg. Allg. Chem.*, 1980, **464**, 255–267.

- 49 K.-P. Xie, W.-J. Xu, C.-T. He, B. Huang, Z.-Y. Du, Y.-J. Su, W.-X. Zhang and X.-M. Chen, *CrystEngComm*, 2016, **18**, 4495–4498.
- 50 M. J. Cliffe, E. N. Keyzer, M. T. Dunstan, S. Ahmad, M. F. L. De Volder, F. Deschler, A. J. Morris and C. P. Grey, *Chem. Sci.*, 2019, **10**, 793–801.
- 51 J. G. Bergman, J. H. McFee and G. R. Crane, *Mater. Res. Bull.*, 1970, **5**, 913–917.
- 52 X. Q. Wang, D. Xu, D. R. Yuan, Y. P. Tian, W. T. Yu, S. Y. Sun, Z. H. Yang, Q. Fang, M. K. Lu, Y. X. Yan, F. Q. Meng, S. Y. Guo, G. H. Zhang and M. H. Jiang, *Mater. Res. Bull.*, 1999, **34**, 2003–2011.
- 53 X.-Q. Wang, D. Xu, M.-K. Lü, D.-R. Yuan, G.-H. Zhang, F.-Q. Meng, S.-Y. Guo and M. Zhou, *Cryst. Res. Technol.*, 2001, **36**, 73–84.
- 54 X. Q. Wang, D. Xu, M. K. Lu, D. R. Yuan, J. Huang, G. W. Lu, G. H. Zhang, S. Y. Guo, H. X. Ning, X. L. Duan, Y. Chen and Y. Q. Zhou, *Opt. Mater.*, 2003, **23**, 335–341.
- 55 J.-L. Do and T. Friščić, *ACS Cent. Sci.*, 2017, **3**, 13–19.
- 56 D. Umeyama, S. Horike, M. Inukai, T. Itakura and S. Kitagawa, *J. Am. Chem. Soc.*, 2015, **137**, 864–870.
- 57 T. D. Bennett and S. Horike, *Nat. Rev. Mater.*, 2018, **3**, 431–440.
- 58 S. Horike, S. S. Nagarkar, T. Ogawa and S. Kitagawa, *Angew. Chem. Int. Ed.*, 2020, **59**, 6652–6664.
- 59 D. L. Smith and V. I. Saunders, *Acta Cryst. B*, 1981, **37**, 1807–1812.
- 60 M. Kabešová, M. Dunaj-jurčo, M. Serator, J. Gažo and J. Garaj, *Inorganica Chim. Acta*, 1976, **17**, 161–165.
- 61 C. Raiß, K. Peppler, J. Janek and P. Adelhelm, *Carbon*, 2014, **79**, 245–255.

- 62 R. A. Bailey, S. L. Kozak, T. W. Michelsen and W. N. Mills, *Coord. Chem. Rev.*, 1971, **6**, 407–445.
- 63 M. Kabešová, J. Kohout and J. Gažo, *Inorganica Chim. Acta*, 1978, **31**, L435–L436.
- 64 R. D. Shannon, *Acta Cryst. A*, 1976, **32**, 751–767.
- 65 S. Zhang and J. Northrup, *Phys. Rev. Lett.*, 1991, **67**, 2339–2342.
- 66 J. E. Northrup and S. B. Zhang, *Phys. Rev. B*, 1994, **50**, 4962–4964.
- 67 R. F. W. Bader, *Atoms in molecules: a quantum theory*, Oxford University Press, Oxford, 1990.
- 68 P. Pattanasattayavong, G. O. Ngongang Ndjawa, K. Zhao, K. W. Chou, N. Yaacobi-Gross, B. C. O'Regan, A. Amassian and T. D. Anthopoulos, *Chem. Commun.*, 2013, **49**, 4154–4156.
- 69 S. S. Nagarkar, H. Kurasho, N. T. Duong, Y. Nishiyama, S. Kitagawa and S. Horike, *Chem. Commun.*, 2019, **55**, 5455–5458.